CrossMark

J⁄M PAPERS

Gill's problem in a sandwiched porous slab

Antonio Barletta[1],†**, Michele Celli**[1]**, Stefano Lazzari**[2] **and Pedro V. Brandão**[1]

[1]Department of Industrial Engineering, Alma Mater Studiorum Università di Bologna,
Viale Risorgimento 2, 40136 Bologna, Italy

[2]Department of Architecture and Design, University of Genoa, Stradone S. Agostino 37,
16123 Genoa, Italy

The classical Gill's stability problem for stationary and parallel buoyant flow in a vertical porous slab with impermeable and isothermal boundaries kept at different temperatures is reconsidered from a different perspective. A three-layer slab is studied instead of a homogeneous slab as in Gill's problem. The three layers have a symmetric configuration where the two external layers have a high thermal conductivity, while the core layer has a much lower conductivity. A simplified model is set up where the thermal conductivity ratio between the external layers and the internal core is assumed as infinite. It is shown that a flow instability in the sandwiched porous slab may arise with a sufficiently large Rayleigh number. It is also demonstrated that this instability coincides with that predicted in a previous analysis for a homogeneous porous layer with permeable boundaries, by considering the limiting case where the permeability of the external layers is much larger than that of the core layer.

Key words: buoyancy-driven instability, convection in porous media

1. Introduction

The occurrence of convection heat transfer in a vertical porous layer saturated by a fluid is a topic that has been widely studied over the last few decades due to its potential interest for several applications. If the main practical use of this knowledge is for the thermal insulation of buildings and for devices such as breathing walls, the topic of convection in vertical porous layers may be important also for geophysics and for the design of filtration systems. The pioneering paper on this topic was that by Gill (1969). This author provided a straightforward and rigorous proof that a vertical porous layer with a homogeneous structure and subjected to a side heating via isothermal boundaries cannot

† Email address for correspondence: antonio.barletta@unibo.it

display a multicellular pattern of convection heat transfer however large the Rayleigh number. This cornerstone result was obtained by modelling the flow through Darcy's law, the Boussinesq approximation and by assuming impermeable isothermal boundaries kept at different temperatures. The analysis carried out by Gill (1969) is grounded on the linear dynamics of perturbations superposed to the steady vertical buoyant flow in a conduction regime induced by a horizontal temperature gradient in the basic state.

The paper by Gill (1969) is the starting point of several later studies including the nonlinear extension of the stability proof (Straughan 1988; Flavin & Rionero 1999), as well as variants involving the Prandtl–Darcy flow model (Rees 1988) and local thermal non-equilibrium within the saturated porous material (Rees 2011; Scott & Straughan 2013).

The use of momentum balance models for the seepage flow in the porous layer that include the velocity Laplacian term shows the possibility of a thermal instability and the emergence of convection patterns in the porous layer (Chen 2004). This feature is an expected consequence of a momentum balance model similar to that for a fluid clear of porous material. In fact, linear convective instability emerges when a vertical and infinitely tall slot of fluid is bounded by impermeable plane walls at different temperatures (Vest & Arpaci 1969). Kwok & Chen (1987) present experimental evidence that convective instability in a vertical porous layer may arise when a sufficiently large temperature difference is forced across the layer boundaries. Those authors also propose possible explanations of the observed phenomenon based either on Brinkman's momentum transfer model or on the inclusion of variable viscosity effects (Kwok & Chen 1987).

The papers by Barletta (2015) and by Shankar & Shivakumara (2022) offer apparently different approaches showing up the emergence of convective instability in a vertical porous slab subjected to side heating. The first one (Barletta 2015) focuses on the same flow set-up assumed by Gill (1969), but turning the impermeability boundary conditions into conditions of permeability by imposing a hydrostatic pressure distribution at the boundaries. The second one (Shankar & Shivakumara 2022) considers a variant of Gill's set-up where the boundaries are impermeable, but the porous medium is heterogeneous with a transverse continuous change of the permeability. Both Barletta (2015) and Shankar & Shivakumara (2022) proved that their variants of Gill's problem could lead to a condition of linear instability for sufficiently large Rayleigh numbers. Further recent explorations into different aspects of the onset of convection in porous vertical layers have been carried out by Barletta & Celli (2021), Shankar, Shivakumara & Naveen (2021) and Shankar, Naveen & Shivakumara (2022).

The aim of this paper is to show that a common physical mechanism underlies the apparently different instabilities found by Barletta (2015) and by Shankar & Shivakumara (2022). This task is achieved by envisaging a three-layer porous slab with impermeable isothermal boundaries kept at different temperatures. In this sandwiched porous slab, the two external layers are identical, while the core layer has different thermophysical properties. In particular, the external layers are considered as much more thermally conductive than the core. The basic buoyant flow in the internal core is identical to that devised by Gill (1969). Although the basic state is stationary with a purely vertical velocity, the core layer has interfaces to the external layers which may allow for a horizontal flow contribution when the basic state is perturbed. This circumstance is a relaxation of Gill's impermeability condition at the boundaries, if just the core layer is considered. Such a set-up is the link between the two studies by Barletta (2015) and Shankar & Shivakumara (2022). In fact, the three-layer structure is effectively a horizontally heterogeneous medium with a piecewise-constant permeability. Furthermore, the internal core is a homogeneous porous layer with permeability conditions at the bounding interfaces to the external layers.
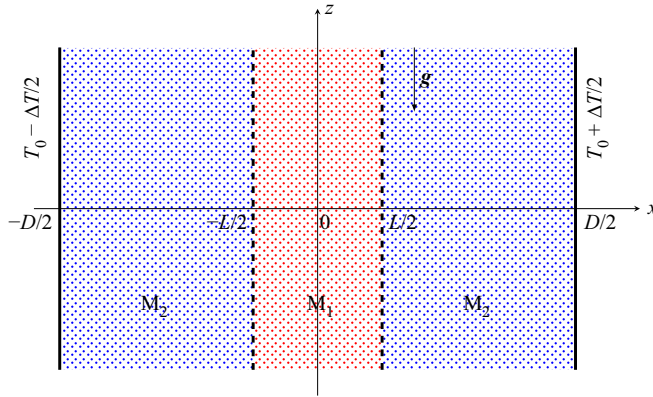
Figure 1. Two-dimensional cross-section of the sandwiched porous slab in the xz plane. The y axis is perpendicular to the plane of the figure.

In this study, it is shown that the neutral stability condition is influenced by the permeability ratio between the external layers and the core layer and by the ratio between the thickness of the three-layer slab and that of the core layer. The role of such parameters in determining the stabilisation or destabilisation of the basic buoyant flow is identified by employing a numerical solution of the linear stability eigenvalue problem. This eigenvalue problem, formulated for the core layer, turns out to coincide with that solved by Barletta (2015) in the asymptotic case where the external layers are much more permeable than the core. Hence, the neutral stability condition and the critical values of the wavenumber and of the Rayleigh number found by Barletta (2015) are confirmed in the asymptotic case. Such an asymptotic condition turns out to be the most unstable relative to cases where the permeability ratio between the external layers and the core layer is finite. It is shown that the stability eigenvalue problem studied by Gill (1969) is recovered in the opposite asymptotic condition where the permeability ratio between the external layers and the core layer tends to zero. This is an expected result as, in this asymptotic case, the interfaces between the core layer and the external layers are effectively impermeable, thus reproducing just the same Gill's boundary conditions for the core layer.

2. Governing equations

Let us consider a vertical porous slab with a sandwiched structure. The x axis is horizontal and perpendicular to the slab, the y axis is also horizontal and the z axis is vertical, so that the gravitational acceleration is $\boldsymbol{g} = -g\,\hat{\boldsymbol{e}}_z$, where g is the modulus of $\boldsymbol{g}$ and $\hat{\boldsymbol{e}}_z$ is the unit vector of the z axis.

As shown in figure 1, the core region $-L/2 \leq x \leq L/2$ is a layer of a porous material M_1, while the regions $-D/2 \leq x < -L/2$ and $L/2 < x \leq D/2$ are layers of a different porous material M_2. For the sake of simplicity, we assume that the slab extends without bounds over the y and z directions. The external boundaries $x = \pm D/2$ are impermeable and isothermal at temperatures $T_0 \pm \Delta T/2$, where T_0 and ΔT are constants, with $\Delta T > 0$.

The flow model is based on the local mass, momentum and energy balance equations according to the Boussinesq approximation and to Darcy's law:

$$\nabla \cdot \boldsymbol{u}_m = 0, \tag{2.1a}$$

$$\frac{\mu}{K_m}\boldsymbol{u}_m = -\nabla P_m + \rho_0 g \beta (T_m - T_0)\hat{\boldsymbol{e}}_z, \tag{2.1b}$$

$$\sigma_m \frac{\partial T_m}{\partial t} + \boldsymbol{u}_m \cdot \boldsymbol{\nabla} T_m = \alpha_m \nabla^2 T_m, \quad m = 1, 2, \tag{2.1c}$$

where the index $m = 1, 2$ identifies the physical properties and the fields either in the core M_1 layer or in the external M_2 layers. Here, t is time, $\boldsymbol{u}_m$ is the velocity field, P_m is the dynamic pressure field and T_m is the temperature field. We emphasise that P_m, the dynamic pressure, is the local difference between the pressure and the hydrostatic pressure, where the latter is evaluated with the reference fluid density ρ_0. The fluid saturating the three-layer slab is Newtonian with a dynamic viscosity μ, a reference density ρ_0 and a coefficient of thermal expansion β.

The average properties of the saturated porous media are, with $m = 1, 2$: the permeability K_m, the thermal diffusivity α_m and the heat capacity ratio σ_m. The latter ratio is evaluated by dividing the volumetric heat capacity of each saturated porous medium by the volumetric heat capacity of the fluid. We also recall that the average thermal diffusivities, α_1 and α_2, are defined through the ratio of the average thermal conductivity of the fluid-saturated porous medium and the volumetric heat capacity of the fluid. The volumetric heat capacity of the fluid is the same for both media M_1 and M_2. Hence, the ratio α_2/α_1 is both a thermal diffusivity ratio and a thermal conductivity ratio.

2.1. *Pressure–temperature formulation*

Equation (2.1) can be expressed in a pressure–temperature formulation:

$$\nabla^2 P_m = \rho_0 g \beta \frac{\partial T_m}{\partial z}, \tag{2.2a}$$

$$\sigma_m \frac{\partial T_m}{\partial t} - \frac{K_m}{\mu} \boldsymbol{\nabla} P_m \cdot \boldsymbol{\nabla} T_m + \frac{\rho_0 g \beta K_m}{\mu}(T_m - T_0)\frac{\partial T_m}{\partial z} = \alpha_m \nabla^2 T_m, \quad m = 1, 2. \tag{2.2b}$$

2.2. *Boundary and interface conditions*

The boundary and interface conditions are to be set at $x = \pm D/2$ and at $x = \pm L/2$, respectively:

$$x = \pm D/2: \quad \frac{\partial P_2}{\partial x} = 0, \quad T_2 = T_0 \pm \frac{\Delta T}{2}, \tag{2.3a}$$

$$x = \pm L/2: \quad P_1 = P_2, \quad K_1 \frac{\partial P_1}{\partial x} = K_2 \frac{\partial P_2}{\partial x}, \quad T_1 = T_2, \quad \alpha_1 \frac{\partial T_1}{\partial x} = \alpha_2 \frac{\partial T_2}{\partial x}. \tag{2.3b}$$

In particular, the interface conditions reflect the momentum and energy balance across the planes at $x = \pm L/2$. They express the continuity of the pressure, of the normal component of the velocity, of the temperature and of the normal component of the heat flux density. The last interface condition (2.3) should employ the thermal conductivities instead of the thermal diffusivities, but we have already pointed out that the ratio α_2/α_1 coincides with the thermal conductivity ratio.

2.3. *Dimensionless formulation*

The mathematical model can be reformulated in dimensionless terms by scaling time, coordinates and fields as

$$t^* = \frac{t}{\sigma_1 L^2/\alpha_1}, \quad (x^*, y^*, z^*) = \frac{(x, y, z)}{L}, \quad \boldsymbol{u}_m^* = \frac{\boldsymbol{u}_m}{\alpha_1/L}, \tag{2.4a}$$

$$P_m^* = \frac{P_m}{\mu \alpha_1 / K_1}, \quad T_m^* = \frac{T_m - T_0}{\Delta T}, \tag{2.4b}$$

with the dimensionless parameters

$$R = \frac{\rho_0 g \beta \Delta T K_1 L}{\mu \alpha_1}, \quad a = \frac{D}{L}, \quad \xi = \frac{K_2}{K_1}, \quad \gamma = \frac{\alpha_2}{\alpha_1} \quad \tau = \frac{\sigma_2}{\sigma_1}. \tag{2.5a–e}$$

Here, $a > 1$ and R is the Darcy–Rayleigh number, hereafter called the Rayleigh number for conciseness. Equations (2.4) and (2.5a–e) allow one to rewrite (2.2) in a dimensionless form for the medium M_1:

$$\nabla^2 P_1 = R \frac{\partial T_1}{\partial z}, \tag{2.6a}$$

$$\frac{\partial T_1}{\partial t} - \boldsymbol{\nabla} P_1 \cdot \boldsymbol{\nabla} T_1 + R T_1 \frac{\partial T_1}{\partial z} = \nabla^2 T_1, \tag{2.6b}$$

and for the medium M_2:

$$\nabla^2 P_2 = R \frac{\partial T_2}{\partial z}, \tag{2.7a}$$

$$\tau \frac{\partial T_2}{\partial t} - \xi \boldsymbol{\nabla} P_2 \cdot \boldsymbol{\nabla} T_2 + R \xi T_2 \frac{\partial T_2}{\partial z} = \gamma \nabla^2 T_2, \tag{2.7b}$$

while (2.3) reads

$$x = \pm a/2: \quad \frac{\partial P_2}{\partial x} = 0, \quad T_2 = \pm \frac{1}{2}, \tag{2.8a}$$

$$x = \pm 1/2: \quad P_1 = P_2, \quad \frac{\partial P_1}{\partial x} = \xi \frac{\partial P_2}{\partial x}, \quad T_1 = T_2, \quad \frac{\partial T_1}{\partial x} = \gamma \frac{\partial T_2}{\partial x}. \tag{2.8b}$$

In (2.6)–(2.8) and in the forthcoming analysis, the dimensionless fields, coordinates and time are denoted without the asterisks for simplicity of notation. This will not cause any ambiguity as we will only deal with dimensionless expressions, except when explicitly declared.

It is also worth saying that the second of equations (2.1) is rewritten in a dimensionless form as

$$\boldsymbol{u}_1 = -\boldsymbol{\nabla} P_1 + R T_1 \hat{\boldsymbol{e}}_z, \tag{2.9a}$$

$$\boldsymbol{u}_2 = -\xi \boldsymbol{\nabla} P_2 + R \xi T_2 \hat{\boldsymbol{e}}_z, \tag{2.9b}$$

for media M_1 and M_2, respectively.

3. The basic stationary flow

A basic stationary flow solution of (2.6)–(2.8) can be found such that

$$\bar{P}_1 = 0 = \bar{P}_2, \quad \frac{\partial \bar{T}_1}{\partial y} = 0 = \frac{\partial \bar{T}_2}{\partial y}, \tag{3.1a,b}$$

where the bar over the fields stands for basic state. Equation (3.1a,b) describes a two-dimensional, y-independent, flow regime where the pressure locally coincides with the hydrostatic pressure or, equivalently, the dynamic pressure is everywhere zero. As a
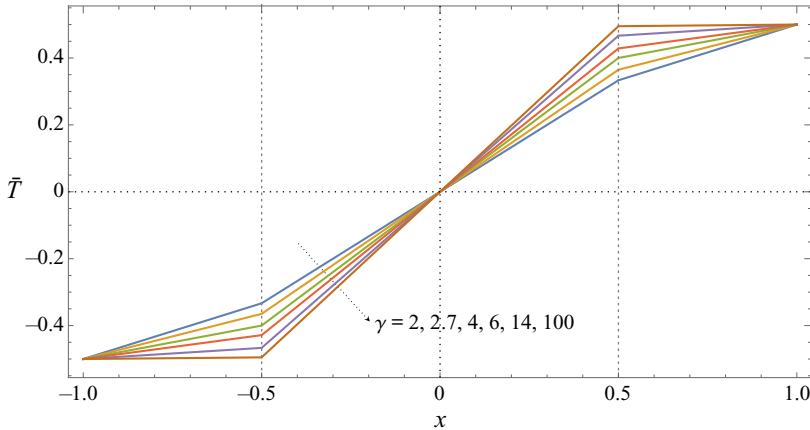
Figure 2. Plots of $\bar{T}$ versus x for $a = 2$ and different values of γ.

consequence of (3.1a,b), (2.6)–(2.8) allow one to infer that, in the three-layer slab, the temperature profile $\bar{T}$ is a piecewise linear function of x independent of y and z. In fact, in the basic state, we have

$$\bar{T}_1 = \frac{\gamma}{\gamma + a - 1} x, \tag{3.2a}$$

$$\bar{T}_2 = \begin{cases} \dfrac{1}{\gamma + a - 1} x - \dfrac{\gamma - 1}{2(\gamma + a - 1)}, & -\dfrac{a}{2} \le x < -\dfrac{1}{2}, \\ \dfrac{1}{\gamma + a - 1} x + \dfrac{\gamma - 1}{2(\gamma + a - 1)}, & \dfrac{1}{2} < x \le \dfrac{a}{2}. \end{cases} \tag{3.2b}$$

Another consequence of (3.1a,b) is that (2.9) yields

$$\bar{u}_1 = (0, 0, R\bar{T}_1), \quad \bar{u}_2 = (0, 0, R\xi\bar{T}_2), \tag{3.3a,b}$$

which describes a purely vertical flow driven only by the buoyancy force. If $\bar{T}$ varies continuously along the range $-a/2 \le x \le a/2$, this is not the case for the vertical velocity component. Such a feature is a consequence of the different permeabilities of the porous media M_1 and M_2, so that continuity of the velocity profile occurs only for the special case $\xi = 1$.

Figure 2 illustrates the basic solution by showing some plots of $\bar{T}$ versus x over the whole range $-a/2 \le x \le a/2$. The geometrical ratio $a = 2$ is prescribed, while different values of the conductivity ratio $\gamma > 1$ are considered. A focus on the case $\gamma > 1$ has been made since, as is discussed in § 3.1, our aim is to explore a condition of extremely high values of γ. It can be stressed that the case $\gamma = 100$ yields a temperature distribution which is almost uniform in the external layers ($-a/2 \le x < -1/2$ and $1/2 < x \le a/2$). This behaviour is characteristic of the asymptotic case $\gamma \to \infty$.

3.1. *Infinite thermal conductivity ratio*

There are several practical cases where the limit $\gamma \to \infty$ is a fairly appropriate condition. Porous media with a very high thermal conductivity are the metal foams often employed in the design of heat exchangers, while the low-conductivity inner core can be devised as a slab of any thermal insulation material employed in the building industry. In the

952 A32-6

forthcoming stability analysis of the basic buoyant flow, we focus on this asymptotic condition. It is worth emphasising that the limit $\gamma \to \infty$ of (3.2) yields

$$\bar{T}_1 = x, \quad \bar{T}_2 = \begin{cases} -\dfrac{1}{2}, & -\dfrac{a}{2} \leq x < -\dfrac{1}{2}, \\ \dfrac{1}{2}, & \dfrac{1}{2} < x \leq \dfrac{a}{2}. \end{cases} \tag{3.4a,b}$$

The basic state (3.4a,b) for the core layer M_1 is exactly that considered in the papers by Gill (1969) and by Barletta (2015). Finally, we reckon that also the governing equations, the boundary and the interface conditions (2.7) and (2.8) undergo a marked simplification:

$$\nabla^2 P_2 = R\frac{\partial T_2}{\partial z}, \quad \nabla^2 T_2 = 0, \tag{3.5a,b}$$

with

$$x = \pm a/2: \quad \frac{\partial P_2}{\partial x} = 0, \quad T_2 = \pm\frac{1}{2}, \tag{3.6a}$$

$$x = \pm 1/2: \quad P_1 = P_2, \quad \frac{\partial P_1}{\partial x} = \xi\frac{\partial P_2}{\partial x}, \quad T_1 = T_2, \quad \frac{\partial T_2}{\partial x} = 0. \tag{3.6b}$$

4. Linearised perturbation dynamics

The onset of instability is studied by perturbing the basic state:

$$P_m = \bar{P}_m + \epsilon\hat{P}_m, \quad T_m = \bar{T}_m + \epsilon\hat{T}_m, \quad m = 1, 2, \tag{4.1a,b}$$

where $\epsilon > 0$ is a perturbation parameter and the hat identifies the perturbation contributions to the pressure and temperature fields. The linear stability analysis is carried out by substituting (4.1a,b) into (2.6), (3.5a,b) and (3.6) and by neglecting the terms $O(\epsilon^2)$. We obtain, for the inner layer M_1,

$$\nabla^2\hat{P}_1 = R\frac{\partial\hat{T}_1}{\partial z}, \quad \frac{\partial\hat{T}_1}{\partial t} - \frac{\partial\hat{P}_1}{\partial x} + Rx\frac{\partial\hat{T}_1}{\partial z} = \nabla^2\hat{T}_1, \tag{4.2a,b}$$

and, for the external layers M_2,

$$\nabla^2\hat{P}_2 = R\frac{\partial\hat{T}_2}{\partial z}, \quad \nabla^2\hat{T}_2 = 0, \tag{4.3a,b}$$

with

$$x = \pm a/2: \quad \frac{\partial\hat{P}_2}{\partial x} = 0, \quad \hat{T}_2 = 0, \tag{4.4a}$$

$$x = \pm 1/2: \quad \hat{P}_1 = \hat{P}_2, \quad \frac{\partial\hat{P}_1}{\partial x} = \xi\frac{\partial\hat{P}_2}{\partial x}, \quad \hat{T}_1 = \hat{T}_2, \quad \frac{\partial\hat{T}_2}{\partial x} = 0. \tag{4.4b}$$

Here, the features of the basic buoyant flow, defined by (3.1a,b) and (3.4a,b), have been employed.

4.1. *Normal mode analysis*

A normal mode expression of the perturbations $(\hat{P}_m, \hat{T}_m)$ is given by

$$\begin{bmatrix} \hat{P}_m \\ \hat{T}_m \end{bmatrix} = \begin{bmatrix} f_m(x) \\ h_m(x) \end{bmatrix} e^{i(k_y y + k_z z - \omega t)}, \quad \text{with } k_y \in \mathbb{R}, k_z \in \mathbb{R}, \omega \in \mathbb{C}, m = 1, 2, \quad (4.5)$$

where $\boldsymbol{k} = (0, k_y, k_z)$ is the wavevector and ω is a complex angular frequency. The wavenumber is a positive quantity defined as the modulus of the wavevector, $k = |\boldsymbol{k}|$. The angular frequency is the real part of ω, while the temporal growth rate is the imaginary part of ω. By substituting (4.5) into (4.2a,b)–(4.4), one obtains for M_1

$$f_1'' - k^2 f_1 - i k_z R h_1 = 0, \quad (4.6a)$$

$$h_1'' - (k^2 - i\omega + i k_z Rx) h_1 + f_1' = 0, \quad (4.6b)$$

and for the external M_2 layers

$$f_2'' - k^2 f_2 - i k_z R h_2 = 0, \quad (4.7a)$$

$$h_2'' - k^2 h_2 = 0, \quad (4.7b)$$

with the boundary and interface conditions

$$x = \pm a/2 : \quad f_2' = 0, \quad h_2 = 0, \quad (4.8a)$$

$$x = \pm 1/2 : \quad f_1 = f_2, \quad f_1' = \xi f_2', \quad h_1 = h_2, \quad h_2' = 0. \quad (4.8b)$$

We can eliminate the dependence on the orientation of the wavevector $\boldsymbol{k}$ in (4.6)–(4.8) by defining a rescaled Rayleigh number, S, such that

$$kS = k_z R. \quad (4.9)$$

Hence, (4.6) and (4.7) read

$$f_1'' - k^2 f_1 - i k S h_1 = 0, \quad (4.10a)$$

$$h_1'' - (k^2 - i\omega + i k S x) h_1 + f_1' = 0 \quad (4.10b)$$

and

$$f_2'' - k^2 f_2 - i k S h_2 = 0, \quad (4.11a)$$

$$h_2'' - k^2 h_2 = 0, \quad (4.11b)$$

respectively.

4.2. *Eigenvalue problem for the core porous layer*

Function h_2 is a solution of the second of equations (4.11) which, on account of (4.8), must satisfy the boundary conditions $h_2(\pm a/2) = 0$. Then, it can be expressed as

$$h_2 = \begin{cases} C_h \sinh\left(k\dfrac{a+2x}{2}\right), & -\dfrac{a}{2} \leq x < -\dfrac{1}{2}, \\ \tilde{C}_h \sinh\left(k\dfrac{a-2x}{2}\right), & \dfrac{1}{2} < x \leq \dfrac{a}{2}, \end{cases} \quad (4.12)$$

where $(C_h, \tilde{C}_h)$ are integration constants. However, (4.8) prescribes also the interface conditions $h_2'(\pm 1/2) = 0$. On account of (4.12), such conditions can be satisfied for $k > 0$

952 A32-8

only with $C_h = 0$ and $\tilde{C}_h = 0$. Hence, one has

$$h_2 = 0. \tag{4.13}$$

Function f_2 must be a solution of the first of equations (4.11) with $h_2 = 0$. Furthermore, on account of (4.8), f_2 satisfies the boundary conditions $f_2'(\pm a/2) = 0$, so that

$$f_2 = \begin{cases} C_f \cosh\left(k\dfrac{a+2x}{2}\right), & -\dfrac{a}{2} \le x < -\dfrac{1}{2}, \\[2mm] \tilde{C}_f \cosh\left(k\dfrac{a-2x}{2}\right), & \dfrac{1}{2} < x \le \dfrac{a}{2}, \end{cases} \tag{4.14}$$

where $(C_f, \tilde{C}_f)$ are integration constants.

Thus, from (4.14), the interface conditions $f_1(-1/2) = f_2(-1/2)$ and $f_1'(-1/2) = \xi f_2'(-1/2)$ given by (4.8) yield

$$f_1\left(-\frac{1}{2}\right) = C_f \cosh\left(k\frac{a-1}{2}\right), \quad f_1'\left(-\frac{1}{2}\right) = C_f \xi k \sinh\left(k\frac{a-1}{2}\right). \tag{4.15a,b}$$

By eliminating C_f, (4.15a,b) yields

$$f_1'\left(-\frac{1}{2}\right) - \xi k \tanh\left(k\frac{a-1}{2}\right) f_1\left(-\frac{1}{2}\right) = 0. \tag{4.16}$$

By employing the same method, the interface conditions $f_1(1/2) = f_2(1/2)$ and $f_1'(1/2) = \xi f_2'(1/2)$ given by (4.8) yield

$$f_1\left(\frac{1}{2}\right) = \tilde{C}_f \cosh\left(k\frac{a-1}{2}\right), \quad f_1'\left(\frac{1}{2}\right) = -\tilde{C}_f \xi k \sinh\left(k\frac{a-1}{2}\right). \tag{4.17a,b}$$

By eliminating $\tilde{C}_f$, (4.17a,b) yields

$$f_1'\left(\frac{1}{2}\right) + \xi k \tanh\left(k\frac{a-1}{2}\right) f_1\left(\frac{1}{2}\right) = 0. \tag{4.18}$$

On account of (4.10), (4.16) and (4.18), one can conclude that the linear stability analysis can be now formulated by focusing just on the inner core region $-1/2 \le x \le 1/2$ and solving the eigenvalue problem

$$f_1'' - k^2 f_1 - ikSh_1 = 0, \tag{4.19a}$$

$$h_1'' - (k^2 - i\omega + ikSx)h_1 + f_1' = 0, \tag{4.19b}$$

$$x = \pm\frac{1}{2}: \quad f_1' \pm \xi k \tanh\left(k\frac{a-1}{2}\right) f_1 = 0, \quad h_1 = 0. \tag{4.19c}$$

After having solved (4.19) and determined f_1, one can determine also f_2 as

$$f_2 = \begin{cases} f_1\left(-\dfrac{1}{2}\right)\left[\cosh\left(k\dfrac{a-1}{2}\right)\right]^{-1} \cosh\left(k\dfrac{a+2x}{2}\right), & -\dfrac{a}{2} \le x < -\dfrac{1}{2}, \\[3mm] f_1\left(\dfrac{1}{2}\right)\left[\cosh\left(k\dfrac{a-1}{2}\right)\right]^{-1} \cosh\left(k\dfrac{a-2x}{2}\right), & \dfrac{1}{2} < x \le \dfrac{a}{2}, \end{cases} \tag{4.20}$$

where (4.14), (4.15a,b) and (4.17a,b) have been used.

4.3. *Features of the stability eigenvalue problem*

We note that (4.16) and (4.18) are boundary conditions of the third kind for f_1. However, they are of a special type as the coefficient of the f_1 term depends on the wavenumber k. A similar circumstance occurs in the linear stability eigenvalue problems solved by Rees & Mojtabi (2013) and by Mohammad, Rees & Mojtabi (2017), where third-kind boundary conditions with a k-dependent coefficient were found for the temperature disturbances. In particular, in Rees & Mojtabi (2013), Prats' problem in a horizontal porous layer (Prats 1966) was reconsidered by studying the effect of the non-zero thermal resistance of the horizontal boundary walls. Thus, from a mathematical viewpoint, the circumstances devised by those authors are comparable with those considered here and leading to (4.19). In fact, we are studying a finite and non-zero hydraulic (instead of thermal) resistance of the external porous layers. We mention that the case of third-kind boundary conditions for the temperature was considered in the analysis of Gill's problem for a vertical plane slab with permeable boundaries by Barletta, Celli & Ouarzazi (2017), while third-kind boundary conditions for the pressure were investigated by Barletta, Celli & Rees (2020). However, in Barletta *et al.* (2017, 2020), the prescribed third-kind conditions feature constant k-independent coefficients, unlike the case defined by (4.19). We mention that third-kind boundary conditions with constant coefficients were also predicted for the pressure field by Nygård & Tyvand (2010).

5. Discussion of the results

The basis for developing the stability analysis is the eigenvalue problem (4.19). Some important characteristics of the onset of instability can be gathered by exploring three significant asymptotic cases.

5.1. *The limit $\xi \to \infty$*

The limiting condition $\xi \to \infty$ embodies the case where the external M_2 layers are much more permeable than the core M_1 layer. We note that the example of metal foams for the M_2 layers is quite close to this condition as such metal foams are generally endowed with a large permeability. In any case, we assume that the large permeability of the M_2 layers is not so large as to suppress the validity of Darcy's law. In this case, the only change in the stability eigenvalue problem is a marked simplification of the boundary conditions. Equation (4.19) thus reads

$$f_1'' - k^2 f_1 - ikSh_1 = 0, \tag{5.1a}$$

$$h_1'' - (k^2 - i\omega + ikSx)h_1 + f_1' = 0, \tag{5.1b}$$

$$x = \pm \frac{1}{2} : \quad f_1 = 0, \quad h_1 = 0. \tag{5.1c}$$

We emphasise that (5.1) coincides with the stability eigenvalue problem for a homogeneous vertical porous layer with permeable boundaries solved by Barletta (2015). This is an important result as the transition to instability in the limiting case $\xi \to \infty$ is defined by the neutral stability data obtained and discussed by Barletta (2015). On taking the limit $\xi \to \infty$, one loses also the dependence on a.

5.2. *The limits $\xi \to 0$ or $a \to 1$*

An asymptotic case completely different from that discussed in § 5.1 is defined by the limit $\xi \to 0$. This limit describes a situation where the M_2 layers are much less permeable than

the core M_1 layer. Strictly speaking, the external layers are quite close to impermeability if compared with the core layer. In this case, (4.19) markedly simplifies to

$$f_1'' - k^2 f_1 - ikSh_1 = 0, \tag{5.2a}$$

$$h_1'' - (k^2 - i\omega + ikSx)h_1 + f_1' = 0, \tag{5.2b}$$

$$x = \pm \frac{1}{2}: \quad f_1' = 0, \quad h_1 = 0. \tag{5.2c}$$

The stability eigenvalue problem (5.2) coincides with that analysed by Gill (1969). This feature is completely unsurprising as Gill (1969) investigated the possible onset of instability in a homogeneous porous layer with impermeable isothermal boundaries kept at different temperatures. Gill (1969) proved that no instability is possible in this case.

It is significant that (5.2) represents also the limiting case $a \to 1$ for any finite ξ. This result is expected as $a \to 1$ means that the thickness of the M_2 layers tends to 0. Thus, one has again a homogeneous porous layer, namely the M_1 layer, with the impermeable boundaries devised in Gill (1969).

5.3. *The limit $a \to \infty$*

When the external M_2 layers have an extremely large thickness, so that $D \gg L$, we have in mind the core M_1 layer surrounded by infinite M_2 media. This condition yields the limit $a \to \infty$ and the stability eigenvalue problem (4.19) simplifies to

$$f_1'' - k^2 f_1 - ikSh_1 = 0, \tag{5.3a}$$

$$h_1'' - (k^2 - i\omega + ikSx)h_1 + f_1' = 0, \tag{5.3b}$$

$$x = \pm \frac{1}{2}: \quad f_1' \pm \xi k f_1 = 0, \quad h_1 = 0. \tag{5.3c}$$

5.4. *The neutral stability curves*

The solution of (4.19) leads to the determination of the neutral stability curves, namely the curves drawn in the (k, S) plane which describe the condition of zero growth rate. In other words, the neutral stability curves are isolines of the imaginary part of the complex parameter ω corresponding to a zero value. Among the many neutral stability curves existing in the (k, S) plane, our attention is focused on that displaying the lowest values of S when input values of a and ξ are prescribed. In fact, the lowest neutral stability curve in the (k, S) plane captures the parametric condition for the initiation of the instability. As this curve usually features an absolute minimum of S for a given k, this minimum yields the threshold for the linear convective instability. The values of k and S for such a minimum are called critical and denoted with k_c and S_c. In order to achieve these results, (4.19) must be solved numerically. There are several techniques available for the solution of stability eigenvalue problems formulated through systems of ordinary differential equations. Comprehensive surveys of and comparisons among the methods are available in Dongarra, Straughan & Walker (1996) and in Straughan & Walker (1996).

Our analysis of the neutral stability curves and of the critical values is carried out by employing a shooting method solution of (4.19) for input values of (a, ξ). The code employed for the implementation of such a method is just an adaptation to the diverse boundary conditions of that described in Barletta (2015). In that paper, the test of the numerical accuracy for this code is also discussed. An alternative and more extensive
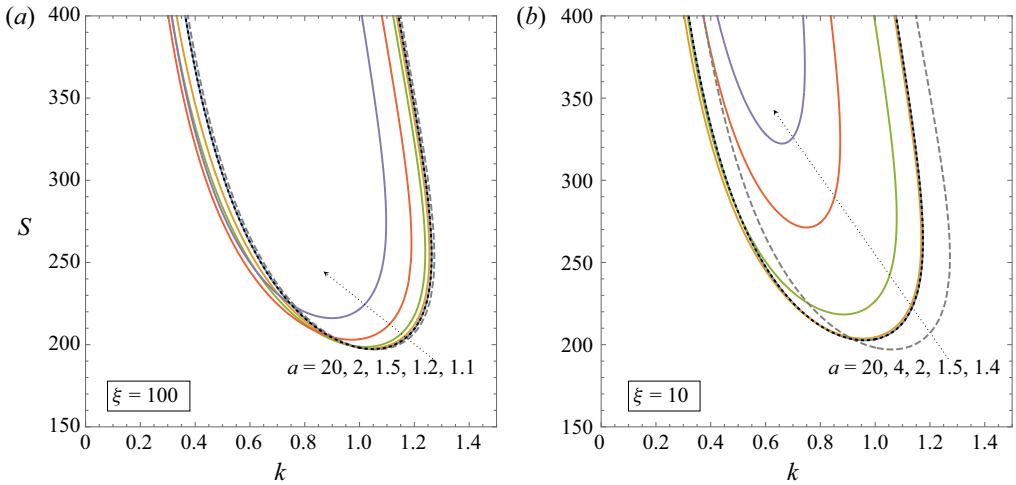
Figure 3. Neutral stability curves in the (k, S) plane for (a) $\xi = 100$ and (b) $\xi = 10$ with different values of a (solid lines). The dashed grey line corresponds to the limit $\xi \to \infty$, while the dotted black line describes the limit $a \to \infty$.

presentation of the shooting method for linear stability eigenvalue problems is also available in Barletta (2019).

It is desirable to see the determined critical value of S, for given (a, ξ), formulated with the Rayleigh number R in order to fully understand the mode selection at the onset of the linear instability. This information is easily gathered from (4.9), as this equation clearly shows that the least value of R_c able to reproduce a given S_c is obtained when $k_z = k$. This means that the preferred modes at the onset of instability are those with $k_y = 0$, the so-called transverse normal modes.

The numerical solution of (4.19) leads to a first important remark: the linear transition to instability occurs with non-travelling modes. This means that the neutral stability curves, defined by a zero imaginary part of ω, are characterised also by a zero real part of ω, so that the phase velocity of the neutrally stable modes is zero. This feature is justified by the numerical solution of the eigenvalue problem (4.19) for several input data (a, ξ).

Figures 3–5 display different frames for different values of ξ. In each frame, the neutral stability curves are displayed for distinct values of a, with the asymptotic case $a \to \infty$ reported for comparison as a dotted black line. Figures 3 and 4 also show the asymptotic case $\xi \to \infty$ as a dashed grey line for a comparison with the situation examined in Barletta (2015). Figure 3, relative to $\xi = 100$ and 10, displays an evident cluttering of the curves close to the asymptote $a \to \infty$ for the largest values of a. For the case $\xi = 100$, the largest values of a mean $a > 1.5$. In this case, there is no visible distinction between the asymptotes $\xi \to \infty$ and $a \to \infty$. We can interpret these findings by saying that, with $\xi = 100$, the analysis carried out in Barletta (2015) yields a fair description of the linear onset of instability for thickness ratios a down to 2 or even smaller. Things are different when $\xi = 10$ as one finds a marked difference between the asymptotes $\xi \to \infty$ and $a \to \infty$. This phenomenon turns out to be even more evident by exploring figure 4 with the cases $\xi = 5$ and $\xi = 2$. In figure 5, relative to $\xi = 1$ and 0.6, the dashed grey line for $\xi \to \infty$ is not even drawn, as such cases are too far from the condition of isobaric boundary conditions, $f_1 = 0$, devised in Barletta (2015).

There is a systematic trend gathered from figures 3–5 which ought to be emphasised. The basic flow tends to be destabilised as a or ξ increases. This conclusion can be inferred
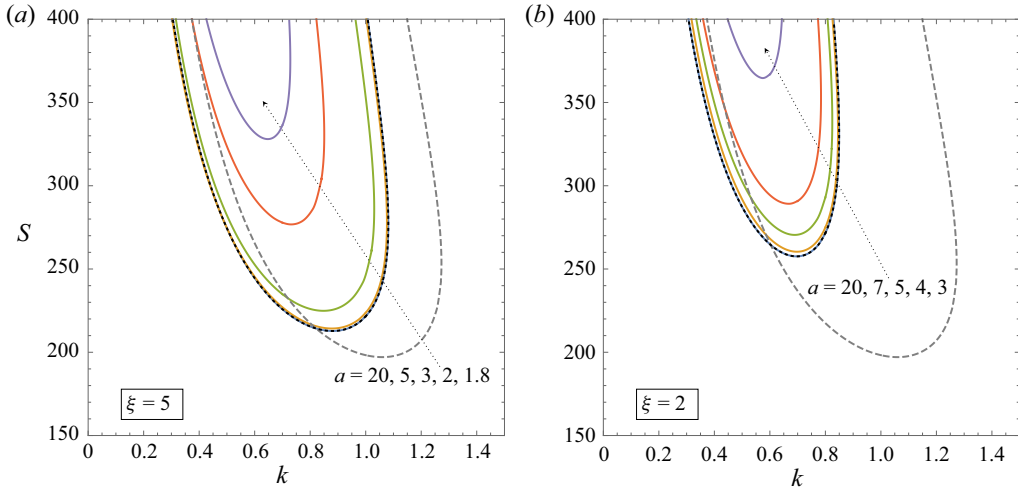
952 A32-12

Figure 4. Neutral stability curves in the (k, S) plane for (*a*) $\xi = 5$ and (*b*) $\xi = 2$ with different values of a (solid lines). The dashed grey line corresponds to the limit $\xi \to \infty$, while the dotted black line describes the limit $a \to \infty$.
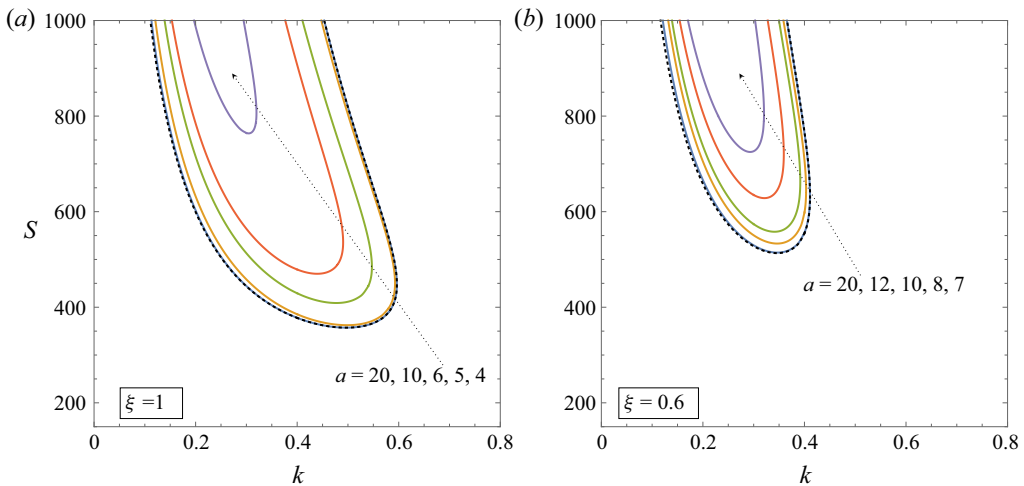

Figure 5. Neutral stability curves in the (k, S) plane for (*a*) $\xi = 1$ and (*b*) $\xi = 0.6$ with different values of a (solid coloured curves). The dotted black curves describe the limit $a \to \infty$.

from figures 3–5 as the neutral stability curve moves upward when the value of either a or ξ decreases. In fact, if the neutral stability curve moves upward, larger and larger values of S are needed to trigger the instability. There is a straightforward interpretation for such a trend. When a gradually decreases, the overall width of the multilayer structure, D, tends to approach the width of the core layer, L. As a consequence, the stabilising effect of the impermeable external boundaries at $x = \pm D/2$, proved by Gill (1969), tends to affect directly the interfaces at $x = \pm L/2$, so that the core layer boundaries become gradually close to impermeability and, hence, to stability for every value of S. Just the same condition happens when the permeability ratio, ξ, tends to zero as demonstrated
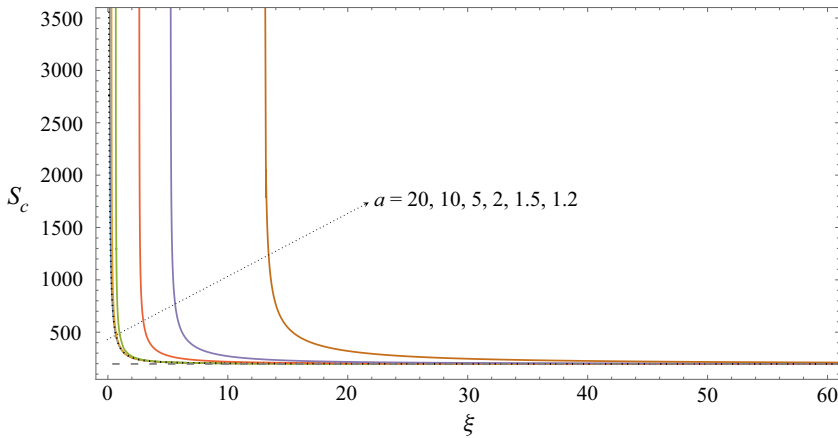
952 A32-13

Figure 6. Critical value of S versus ξ for a decreasing from 20 to 1.2 (solid coloured curves). The dotted black curve describes the limit $a \to \infty$, while the dashed grey line denotes the asymptotic value for $\xi \to \infty$, $S_c = 197.0812$.

mathematically in § 5.2. It is also evident from figures 3–5 that the instability tends to be caused by smaller and smaller wavenumbers, k, for decreasing values of either a or ξ.

5.5. *Critical conditions for the instability*

The minimum of the neutral stability curve in the (k, S) plane identifies the onset of the linear instability, with the least value of S needed for the convection cells to display a growing amplitude in time. Such a minimum identifies the critical values $k = k_c$ and $S = S_c$, which depend on both a and ξ. The critical data are presented graphically in figures 6 and 7 where the trends of S_c and k_c versus ξ are displayed. These figures reveal that the cases $a = 20$, 10, 5 yield hardly distinguishable curves almost overlapped with the asymptotic dotted black line corresponding to the limit $a \to \infty$. A departure from this behaviour is found only for small values of ξ in a range where the singularity of S_c is displayed in figure 6 with a steep increase of the critical value of S as ξ decreases. We also report that the asymptotic regime $\xi \to \infty$ is approached by S_c more and more rapidly the larger is the value of a. Thus, one can say that the case examined by Barletta (2015) is one naturally emerging when both a and ξ are large enough. For instance, a glance at figure 6 may suggest $a \geq 5$ and $\xi \geq 20$ as a possible indication where the model of permeable boundaries employed by Barletta (2015) can be considered as a fair enough approximation for practical purposes. Figures 6 and 7 also reveal that, for every $a > 0$, S_c becomes infinite and k_c becomes zero when $\xi \to \xi_a > 0$. The constant ξ_a is a decreasing function of a. The evaluation of ξ_a is achieved by the solution of the stability eigenvalue problem in a large-S range where the accuracy of the numerical solver significantly decreases. A few values of ξ_a relative to the values of a considered in figures 6 and 7 are shown in table 1. Only three significant figures could be reported in this table due to the mentioned decrease in numerical accuracy. An important result is that no linear instability is found when $\xi \leq \xi_a$.

Critical values $k = k_c$ and $S = S_c$ are given in tables 2 and 3 versus ξ for different decreasing values of a, from the asymptotic condition $a \to \infty$ to $a = 1.2$. Critical data are not reported for the cases where $\xi \leq \xi_a$. In fact, as pointed out above, a threshold to instability is found only for a ξ larger than ξ_a.
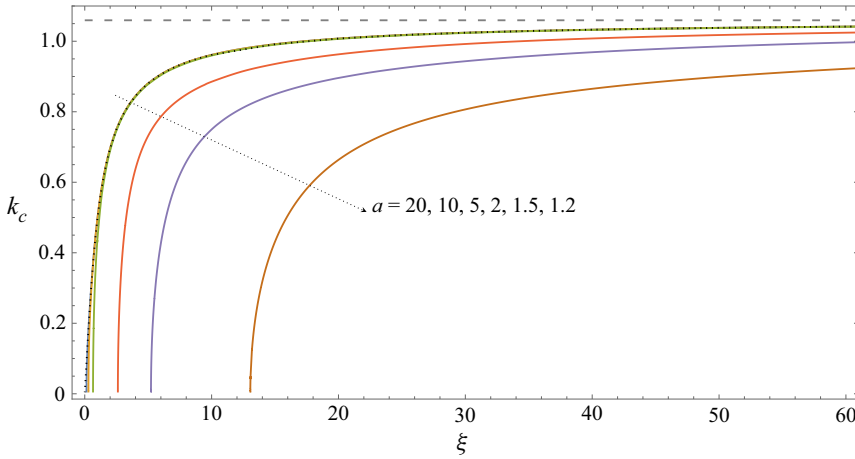
952 A32-14

Figure 7. Critical value of k versus ξ for a decreasing from 20 to 1.2 (solid coloured curves). The dotted black curve describes the limit $a \to \infty$, while the dashed grey line denotes the asymptotic value for $\xi \to \infty$, $k_c = 1.059498$.

a	ξ_a
∞	0.000
20	0.138
10	0.290
5	0.653
2	2.61
1.5	5.22
1.2	13.0

Table 1. Values of ξ_a versus a.

	$a \to \infty$		$a = 20$		$a = 10$		$a = 5$	
ξ	k_c	S_c	k_c	S_c	k_c	S_c	k_c	S_c
0.6	0.346043	513.2325	0.346630	514.3766	0.341008	557.9773	—	—
0.8	0.428912	413.6608	0.429127	413.8280	0.429635	426.9214	0.309628	724.4452
1	0.496592	357.2767	0.496672	357.3117	0.498337	362.4913	0.439495	470.0357
2	0.696054	257.5909	0.696056	257.5912	0.696745	257.9235	0.689313	270.4812
5	0.880580	212.7840	0.880580	212.7840	0.880638	212.8010	0.878152	214.2687
10	0.961336	202.6737	0.961336	202.6737	0.961338	202.6766	0.959440	203.0420
20	1.007717	199.1513	1.007717	199.1513	1.007714	199.1520	1.006539	199.2567
50	1.038056	197.7046	1.038056	197.7046	1.038054	197.7047	1.037528	197.7294
100	1.048649	197.3556	1.048649	197.3556	1.048647	197.3557	1.048375	197.3653
∞	1.059498	197.0812	1.059498	197.0812	1.059498	197.0812	1.059498	197.0812

Table 2. Critical values of k and S.

5.6. *Streamlines and isotherms*

The visualisation of the streamlines and isotherms associated with the perturbation modes is quite important, especially at the critical conditions $k = k_c$ and $S = S_c$ defining the initiation of the convective instability. In fact, even if the flow patterns of convection

	$a = 2$		$a = 1.5$		$a = 1.2$	
ξ	k_c	S_c	k_c	S_c	k_c	S_c
5	0.731871	276.7961	—	—	—	—
10	0.885192	218.3671	0.749783	271.2792	—	—
20	0.962897	203.7273	0.895889	216.6798	0.663605	320.8838
30	0.992229	200.6034	0.943341	206.8434	0.806683	246.7193
40	1.007888	199.3752	0.968895	203.1681	0.865160	225.6955
50	1.017638	198.7474	0.985154	201.3538	0.898999	216.2033
60	1.024293	198.3750	0.996456	200.3078	0.921864	210.9843
80	1.032791	197.9620	1.011160	199.1856	0.951664	205.6243
100	1.037986	197.7425	1.020310	198.6121	0.970623	203.0113
∞	1.059498	197.0812	1.059498	197.0812	1.059498	197.0812

Table 3. Critical values of k and S.

are evaluated according to the linear theory, it is generally retained that such patterns are the starting point for the development of the nonlinear analysis of convection. This is particularly evident in the formulation of the weakly nonlinear theory of convective instability (Drazin & Reid 2004). In fact, the weakly nonlinear theory studies the interaction between normal modes in the vicinity of the critical condition.

Starting from (2.9) and (4.1a,b), one can define the perturbation velocity:

$$\hat{\boldsymbol{u}}_1 = -\nabla \hat{P}_1 + R\hat{T}_1 \hat{\boldsymbol{e}}_z, \tag{5.4a}$$

$$\hat{\boldsymbol{u}}_2 = -\xi \nabla \hat{P}_2 + R\xi \hat{T}_2 \hat{\boldsymbol{e}}_z. \tag{5.4b}$$

We mentioned that the onset of instability occurs with transverse modes, i.e. the two-dimensional perturbations in the (x, z) plane with $k_y = 0$ and $k = k_z$. Accordingly, only the velocity components $(\hat{u}_m, \hat{w}_m)$, with $m = 1, 2$, are non-zero for such modes. The mass balance constrains $\hat{\boldsymbol{u}}_m$ to be solenoidal. Thus, one can introduce the streamfunction $\hat{\Psi}_m$, so that the divergence of $\hat{\boldsymbol{u}}_m$ is identically zero:

$$\hat{u}_m = \frac{\partial \hat{\Psi}_m}{\partial z}, \quad \hat{w}_m = -\frac{\partial \hat{\Psi}_m}{\partial x}. \tag{5.5a,b}$$

Following (4.5), we express the streamfunction as a normal mode:

$$\hat{\Psi}_m = \psi_m(x)\, e^{i(kz - \omega t)}. \tag{5.6}$$

Then, (4.5) and (5.4)–(5.6) yield

$$ik\psi_1(x) = -f_1'(x), \quad -\psi_1'(x) = -ikf_1(x) + Rh_1(x), \tag{5.7a,b}$$

$$ik\psi_2(x) = -\xi f_2'(x), \quad -\psi_2'(x) = -ik\xi f_2(x) + R\xi h_2(x). \tag{5.7c,d}$$

As a consequence, the interface conditions at $x = \pm 1/2$ expressed by (4.8) imply a continuity of ψ_m across such interfaces with a discontinuity in its first derivative when $\xi \neq 1$:

$$x = \pm 1/2: \quad \psi_1 = \psi_2, \quad \xi \psi_1' = \psi_2'. \tag{5.8a,b}$$

By employing (5.6) and (5.8), one realises that $\nabla \hat{\Psi}_m$ undergoes a cusp discontinuity at each interface where its x component changes discontinuously, if $\xi \neq 1$, while the z component
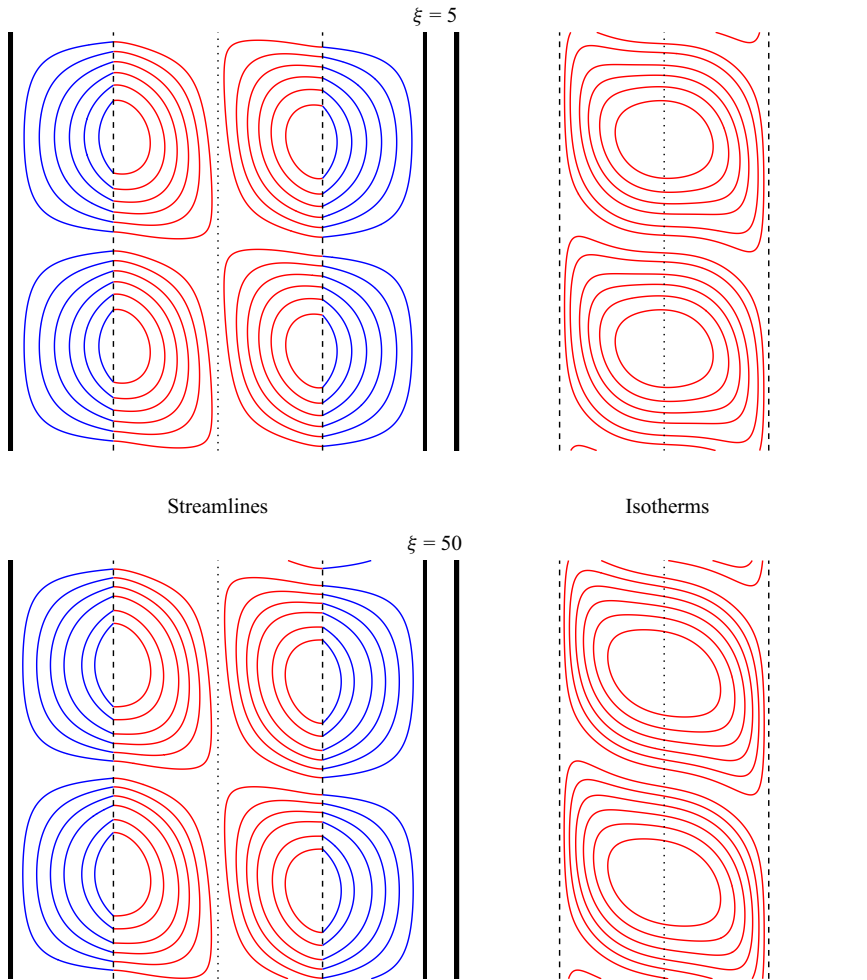
952 A32-16

Figure 8. Perturbation streamlines and isotherms for transverse modes ($k_y = 0$, $k_z = k$ and $S = R$) with $a = 2$ and either $\xi = 5$ or $\xi = 50$, at critical conditions $k = k_c$ and $R = S = S_c$. The dotted black line is at $x = 0$, while the dashed lines denote the interfaces $x = \pm 1/2$. The vertical range is over a period $0 \leq z \leq 2\pi/k_c$.

is always continuous. Such cusp discontinuities of the streamlines at the interfaces are clearly visible in figures 8 and 9, except for the case $a = 5$ and $\xi = 1$ reported in the upper part of figure 9. These figures illustrate just four sample cases in order to display how the convective instability induces a cellular flow which penetrates the M_2 layers. In such external layers, the saturated porous medium is otherwise isothermal, at equilibrium with the external impermeable boundaries, $x = \pm a/2$. The latter feature emerges quite clearly from figures 8 and 9 as the cellular patterns for the isotherms are entirely confined in the core M_1 layer, that is, within the region $-1/2 \leq x \leq 1/2$. The red/blue colour code for the different media introduced in figure 1 is used also in figures 8 and 9 for convenience. We finally point out that the antisymmetry of the convection cells with respect to the vertical midplane reflects the antisymmetric thermal boundary conditions and the antisymmetric basic temperature profile triggering the onset of the convection cells.
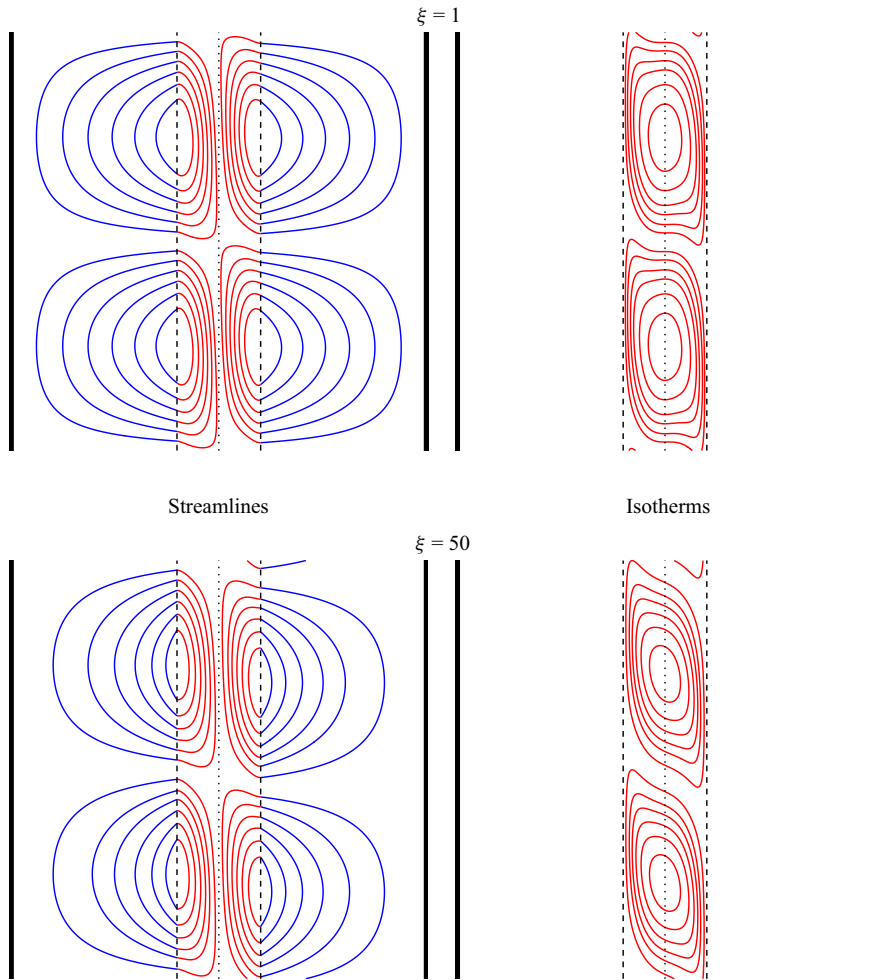
$\xi = 1$

Streamlines   Isotherms

$\xi = 50$

Figure 9. Perturbation streamlines and isotherms for transverse modes ($k_y = 0$, $k_z = k$ and $S = R$) with $a = 5$ and either $\xi = 1$ or $\xi = 50$, at critical conditions $k = k_c$ and $R = S = S_c$. The dotted black line is at $x = 0$, while the dashed lines denote the interfaces $x = \pm 1/2$. The vertical range is over a period $0 \le z \le 2\pi/k_c$.

6. Conclusions

The onset of convection in a vertical porous slab has been analysed by assuming a three-layer structure. In fact, an internal layer is sandwiched between two identical external layers having properties different from those of the core. The multilayer slab is saturated by a Newtonian fluid and the external layers are much more thermally conductive than the inner core. The multilayer slab is bounded by impermeable isothermal walls kept at different temperatures.

The dynamics of convection is governed by Darcy's law and by the thermal buoyancy modelled through the Boussinesq approximation. Being extremely conductive, the external layers are thermally passive but they can be penetrated by the convection cells arising in the core layer. The basic state features a vertical flow, with a piecewise-linear velocity profile, in a thermal conduction regime. Such a basic state reproduces in the inner layer that envisaged by both Gill (1969) and Barletta (2015). Those authors considered

952 A32-18

a single-layer homogeneous slab with either impermeable boundaries (Gill 1969) or permeable boundaries (Barletta 2015).

The linear perturbations of the basic flow have been studied by employing a modal analysis. The neutral stability curves have been obtained in the (k, S) plane, where k is the wavenumber and S is a suitably rescaled Rayleigh number, which coincides with the Rayleigh number R in the special case of two-dimensional transverse modes. The neutral stability condition depends on two governing parameters: the permeability ratio of the outer layers to the inner layer, ξ; and the width ratio of the whole slab to the inner layer, a. The critical conditions $k = k_c$ and $S = S_c$, corresponding to the point of minimum S along a neutral stability curve, have been also evaluated.

The main results obtained from the linear stability analysis are the following:

- The most unstable perturbation modes are transverse. The transverse modes are two-dimensional lying in the vertical (x, z) plane, where the x axis is horizontal and perpendicular to the slab and the z axis is vertical.
- The basic flow is destabilised by both the increase of a and the increase of ξ. The most unstable parametric set-up is the limiting case $\xi \to \infty$, where the neutral stability condition is not influenced by the value of a as the stability eigenvalue problem coincides with that laid out and solved by Barletta (2015).
- For every value of a, there exists a positive constant ξ_a such that no linear instability is found for $\xi \leq \xi_a$. The constant ξ_a is a decreasing function of a.
- The limiting case $\xi \to 0$ drives the basic flow to linear stability for every a and for every Rayleigh number. Such an asymptotic condition is that devised in the rigorous proof of stability presented by Gill (1969) in his classic paper. The interfaces between the internal layer and the external layers become, in fact, perfectly impermeable in this case.
- Since the external layers have a thermal conductivity much larger than that of the core layer, they are isothermal with the same temperature as the neighbouring boundary. This happens both for the basic state and for the perturbed flow. Thus, the external layers are thermally passive at onset of instability. When the convection cells emerge at supercritical conditions, the streamlines of such cells penetrate the external layers showing up cusp discontinuities at the interfaces. The origin of the cusp discontinuities relies on the difference between the permeability of the external layers relative to that of the core layer.

The analysis carried out in this paper points out that the multilayer structure of a vertical porous slab with impermeable isothermal boundaries may induce the onset of convective instability whereas a single-layer vertical slab with the same boundary conditions displays no instability. This result points out a new connection between two apparently different types of instability: the instability in a vertical porous slab with a heterogeneous permeability structure and that in a homogeneous vertical slab with permeable boundaries. The former case, relative to a continuous type of heterogeneity, has been examined by Shankar & Shivakumara (2022). On the other hand, the latter case is retrieved from our analysis when the asymptotic condition $\xi \to \infty$ is examined, perfectly matching the mathematical formulation and the numerical results presented in Barletta (2015).

Declaration of interests. The authors report no conflict of interest.

Author ORCIDs.

Antonio Barletta https://orcid.org/0000-0002-6994-5585;

Michele Celli https://orcid.org/0000-0002-2726-4175;

Stefano Lazzari https://orcid.org/0000-0002-0832-7601;

Pedro V. Brandão https://orcid.org/0000-0002-8445-3802.

REFERENCES

BARLETTA, A. 2015 A proof that convection in a porous vertical slab may be unstable. *J. Fluid Mech.* **770**, 273–288.

BARLETTA, A. 2019 *Routes to Absolute Instability in Porous Media*. Springer.

BARLETTA, A. & CELLI, M. 2021 Anisotropy and the onset of the thermoconvective instability in a vertical porous layer. *Trans. ASME J. Heat Transfer* **143**, 102601.

BARLETTA, A., CELLI, M. & OUARZAZI, M.N. 2017 Unstable buoyant flow in a vertical porous layer with convective boundary conditions. *Intl J. Therm. Sci.* **120**, 427–436.

BARLETTA, A., CELLI, M. & REES, D.A.S. 2020 On the stability of parallel flow in a vertical porous layer with annular cross section. *Transp. Porous Media* **134**, 491–501.

CHEN, Y.-C. 2004 Non-Darcy flow stability of mixed convection in a vertical channel filled with a porous medium. *Intl J. Heat Mass Transfer* **47**, 1257–1266.

DONGARRA, J.J., STRAUGHAN, B. & WALKER, D.W. 1996 Chebyshev tau-QZ algorithm methods for calculating spectra of hydrodynamic stability problems. *Appl. Numer. Maths* **22**, 399–434.

DRAZIN, P.G. & REID, W.H. 2004 *Hydrodynamic Stability*. Cambridge University Press.

FLAVIN, J.N. & RIONERO, S. 1999 Nonlinear stability for a thermofluid in a vertical porous slab. *Contin. Mech. Thermodyn.* **11**, 173–179.

GILL, A.E. 1969 A proof that convection in a porous vertical slab is stable. *J. Fluid Mech.* **35**, 545–547.

KWOK, L.P. & CHEN, C.F. 1987 Stability of thermal convection in a vertical porous layer. *Trans. ASME J. Heat Transfer* **109**, 889–893.

MOHAMMAD, A.N., REES, D.A.S. & MOJTABI, A. 2017 The effect of conducting boundaries on the onset of convection in a porous layer which is heated from below by internal heating. *Transp. Porous Media* **117**, 189–206.

NYGÅRD, H.S. & TYVAND, P.A. 2010 Onset of convection in a porous box with partly conducting and partly penetrative sidewalls. *Transp. Porous Media* **84**, 55–73.

PRATS, M. 1966 The effect of horizontal fluid flow on thermally induced convection currents in porous mediums. *J. Geophys. Res.* **71**, 4835–4838.

REES, D.A.S. 1988 The stability of Prandtl-Darcy convection in a vertical porous layer. *Intl J. Heat Mass Transfer* **31**, 1529–1534.

REES, D.A.S. 2011 The effect of local thermal nonequilibrium on the stability of convection in a vertical porous channel. *Transp. Porous Media* **87**, 459–464.

REES, D.A.S. & MOJTABI, A. 2013 The effect of conducting boundaries on Lapwood-Prats convection. *Intl J. Heat Mass Transfer* **65**, 765–778.

SCOTT, N.L. & STRAUGHAN, B. 2013 A nonlinear stability analysis of convection in a porous vertical channel including local thermal nonequilibrium. *J. Math. Fluid Mech.* **15**, 171–178.

SHANKAR, B.M., NAVEEN, S.B. & SHIVAKUMARA, I.S. 2022 Stability of double-diffusive natural convection in a vertical porous layer. *Transp. Porous Media* **141**, 87–105.

SHANKAR, B.M. & SHIVAKUMARA, I.S. 2022 Gill's stability problem may be unstable with horizontal heterogeneity in permeability. *J. Fluid Mech.* **943**, A20.

SHANKAR, B.M., SHIVAKUMARA, I.S. & NAVEEN, S.B. 2021 Density maximum and finite Darcy-Prandtl number outlooks on Gill's stability problem subject to a lack of thermal equilibrium. *Phys. Fluids* **33**, 124108.

STRAUGHAN, B. 1988 A nonlinear analysis of convection in a porous vertical slab. *Geophys. Astrophys. Fluid Dyn.* **42**, 269–275.

STRAUGHAN, B. & WALKER, D.W. 1996 Two very accurate and efficient methods for computing eigenvalues and eigenfunctions in porous convection problems. *J. Comput. Phys.* **127**, 128–141.

VEST, C.M. & ARPACI, V.S. 1969 Stability of natural convection in a vertical slot. *J. Fluid Mech.* **36**, 1–15.